2024-07-15

# Comparing thin and volume regimes of analog holograms for wavefront sensing

Emma Branigan
*Technological University Dublin*, emma.branigan@tudublin.ie

Andreas Zepp
*Fraunhofer Institute of Optronics, System Technologies and Image Exploitation*, andreas.zepp@iosb.fraunhofer.de

Suzanne Martin
*Technological University Dublin*, suzanne.martin@tudublin.ie

*See next page for additional authors*

## Recommended Citation

Branigan, Emma; Zepp, Andreas; Martin, Suzanne; Sheehan, Matthew; Gladysz, Szymon; and Murphy, Kevin, "Comparing thin and volume regimes of analog holograms for wavefront sensing" (2024). *Articles*. 110.
https://arrow.tudublin.ie/cieoart/110

Funder: Science Foundation Ireland

## Authors

Emma Branigan, Andreas Zepp, Suzanne Martin, Matthew Sheehan, Szymon Gladysz, and Kevin Murphy

Research Article Vol. 32, No. 16 / 29 Jul 2024 / Optics Express 27239

Optics EXPRESS

# Comparing thin and volume regimes of analog holograms for wavefront sensing

**Emma Branigan,**[1,3] **Andreas Zepp,**[2] **Suzanne Martin,**[1] **Matthew Sheehan,**[1] **Szymon Gladysz,**[2] **and Kevin Murphy**[1,*]

[1] *Centre for Industrial and Engineering Optics, School of Physics, Clinical and Optometric Sciences, Technological University Dublin (TU Dublin), D07 ADY7 Dublin, Ireland*
[2] *Fraunhofer IOSB, Ettlingen, Fraunhofer Institute of Optronics, System Technologies and Image Exploitation, Gutleuthausstr. 1, 76275 Ettlingen, Germany*
[3] *emma.branigan@tudublin.ie*
[*] *kevin.p.murphy@tudublin.ie*

**Abstract:** Two analog holographic wavefront sensors, for measurement of defocus, have been fabricated as both thin and volume phase transmission holograms in a self-developing photopolymer. This represents the first reported direct comparison of hologram regimes when designed for wavefront sensing. An analysis of the effect of crosstalk in the presence of one other aberration mode (astigmatism X (0/90°), coma X (horizontal), and primary spherical aberration) was carried out with each version of the sensor. The performance of thin and volume analog holographic wavefront sensors was characterized under emulated conditions associated with moderate atmospheric turbulence.

## 1. Introduction

The holographic wavefront sensor (HWFS) is an implementation of modal wavefront sensing theory presented by Neil *et al.* in 2000 [1]. This modal wavefront sensing method is based on a phase biasing approach, in which a holographic diffraction grating is biased with a phase delay/advance associated with a known magnitude for a specific aberration mode. A pair of holograms are required to sense each mode. The magnitude of the aberration mode contained in an incident wavefront is quantified through a measurement of the intensities of the diffracted beams from the hologram pair. Many variations of the HWFS have been produced through both analog [2–9] and digital [10–14] holographic techniques. Both thin and volume holographic diffraction gratings have been used for holographic wavefront sensing. Typically, reflection spatial light modulators (SLM) are used to display computer generated holograms for digital holographic wavefront sensing (DHWFS), which are thin holograms. Surface relief holograms, created using photolithographic techniques [15], have been used and also function as thin gratings. Thin and volume phase transmission holograms have been recorded in materials such as silver halide [10,16], dichromated gelatin [8], and an acrylamide-based photopolymer [9,17] for the fabrication of an analog holographic wavefront sensor (AHWFS). However, the *regime* (thin, volume, or mixed) in which the hologram operates has historically received little consideration. The diffraction behavior of the hologram is dependent on the regime of operation. Thin holographic gratings produce many diffracted orders, similar to classical diffraction gratings. Volume holographic gratings redirect light into a single order only. Whether the sensor is implemented through thin or volume holography has many implications including; the type of holographic recording materials that are suitable, the ability to multiplex, the environment of deployment, and photon efficiency. Cognisant of these implications of operating in either

#527893 https://doi.org/10.1364/OE.527893
Journal © 2024 Received 26 Apr 2024; revised 4 Jul 2024; accepted 5 Jul 2024; published 15 Jul 2024

regime, an examination of the effect of crosstalk with regards to thin and volume holograms for holographic wavefront sensing is presented. For the work presented here, a thin analog hologram was used in place of an SLM to allow for direct comparison between thin and volume AHWFSs, however it is directly analogous to its digital relative. While the method used for wavefront sensing is applicable to both thin and volume versions of the sensor, the fundamental theory describing each regime is not.

The issue of intermodal crosstalk has been highlighted in many works in the field of holographic wavefront sensing and some authors have developed novel strategies to mitigate its effect [18,19]. Intermodal crosstalk is an unwanted effect that occurs when many aberrations are present in an incoming beam and impairs the measurement accuracy of the HWFS. For applications in adaptive optics (AO), wavefront measurement inaccuracy will lead to inaccurate wavefront correction. This work aims to demonstrate the differences and highlight the advantages/disadvantages of using thin and volume holograms for analog holographic wavefront sensing.

A brief discussion behind the holographic regimes and the conditions required to fabricate thin and volume phase transmission holograms is presented. The methods used to fabricate thin and volume analog holograms in Bayfol HX200, a self-developing photopolymer, are described. Crosstalk effects in the thin and volume AHWFSs were first characterized by measurement of defocus ($Z_2^0$) in combination with just one other aberration mode: astigmatism X (0/90°) ($Z_2^2$), coma X (horizontal) ($Z_3^1$), and primary spherical aberration ($Z_4^0$). Then, uncorrelated phase screens, emulating moderate atmospheric turbulence, were applied to an SLM, along with a fixed magnitude of $Z_2^0$, and the resulting wavefront was measured by the AHWFSs in the presence of multiple aberration modes. Two methods were used to measure the diffracted beam intensities from the holograms; photodiodes and a camera with a software-defined circular region of interest (ROI).

## 2. Theory

### 2.1. Holographic wavefront sensor

A paired set of holograms, $H_1$ and $H_2$, is required for the measurement of a single aberration mode with a HWFS. Thin and volume analog holographic gratings for wavefront sensing are fabricated by similar methods. Whether the hologram operates in the thin or volume regime is dependent on the recording arrangement and recording material properties. A photopolymer-based phase transmission holographic grating is constructed when two coherent light beams overlap at the plane of the holographic recording material and produce a modulation in the refractive index of the material. In regions where constructive interference occurs, polymer fringes are formed by photopolymerization. The spatial frequency of the grating is a measure of how often the photonic structure repeats throughout the holographic optical element (HOE). The polymer fringes can be unslanted or slanted in the material, depending on the holographic recording geometry. For the purpose of this work, only slanted gratings were considered.

To construct a hologram for wavefront sensing ($H_1$), one of the two recording beams must contain a bias aberration with a known sign and magnitude. Typically, this is the beam at normal incidence to the plane of the recording material. For efficiency and elegance, a second hologram ($H_2$) containing the same bias magnitude, but of opposite sign, can be holographically angularly multiplexed on top of the first. However, this multiplexing step is not always necessary and wavefront sensing can be carried out with two separate holographic recordings, and with asymmetric bias magnitudes. For both thin and volume versions of the sensor, the wavefront aberration information is contained in the first diffracted order.

An initial characterization step is required to obtain a calibrated response from the AHWFS. When the hologram is replayed with a beam containing the same bias aberration but of a different magnitude the beam is only partially diffracted into the first order. A normalized ratio of intensities (*NIR*) of the first-order diffracted beams from the pair of wavefront sensing holograms, associated with a given aberration mode, is used to produce the sensor characteristic curve (Fig. 1). The normalized intensity ratio is calculated by Eq. 1

$$NIR = \frac{I_{H1} - I_{H2}}{I_{H1} + I_{H2}}. \tag{1}$$

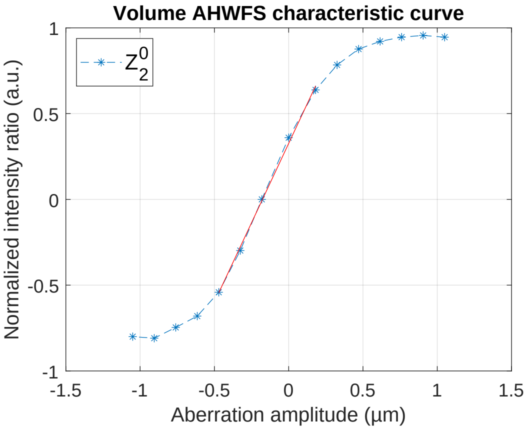

**Fig. 1.** Characteristic curve for a volume AHWFS, for measurement of $Z_2^0$ in the range ± 1.05 µm. The *NIR* was calculated over a software ROI, radius = 62 pixels. Red line indicates the portion of the curve over which the slope, $m_{CC}$, is calculated.

In order to calculate the magnitude of the aberration, $W_D$, contained in an incident wavefront the *NIR* must be divided by the slope of the central, approximately linear region of the characteristic curve, $m_{CC}$ (Eq. 2)

$$W_D = \frac{NIR}{m_{CC}}. \tag{2}$$

A change in the aberration magnitude causes a change in the spatial distribution of the diffracted first-order spots from both the thin and volume AHWFS. In addition there is a large change in the diffraction efficiency (DE) of the first diffracted order from the volume holograms. However, there is no measurable change in the DE of the first-order from the thin AHWFS, as the angular selectivity of thin holograms is low. While it is possible to obtain a measurement of the wavefront using the entirety of the diffracted spots from a volume AHWFS, this is not the case with a thin AHWFS. The ROI over which the *NIR* is calculated must be optimized based on the chosen bias aberration [8,19].

### 2.2. *Classification of volume and thin holograms*

The ratio of fringe spacing, Λ, to material layer thickness, *d*, is an important factor that determines the diffraction behavior of the hologram. For volume holograms or thick holograms, the thickness of the recording material is generally much larger than the mean spacing of the interference fringes, DE can be up to 100%, and diffraction occurs into the first order only. The diffraction behavior follows Bragg's law of diffraction (Eq. 3) and the hologram is only fully reconstructed when the exact Bragg condition, $\theta_B$, used in the recording process is satisfied.

$$m\lambda_r = 2\Lambda\sin\theta_B \tag{3}$$

where $m$ is the diffraction order and $\lambda_r$ is the wavelength of the beam used to replay the hologram. Plane or thin holograms are recorded when the recording material thickness is less than the mean spacing of the interference fringes. These holograms behave like typical diffraction gratings, where incident radiation is diffracted into multiple orders at once and the achievable DE in the first order is relatively low at <33.9% [20].

The Klein & Cook $Q$ parameter [21] is a well-known identifier of the regime in which a hologram operates (Eq. (4)).

$$Q = \frac{2\pi\lambda_r d}{n\Lambda^2} \tag{4}$$

where $\lambda_r$ is the wavelength of the beam used to replay the hologram, $d$ is the material layer thickness, and $n$ is the average refractive index of the medium. A $Q$ value of $>10$ is indicative of the volume regime and a $Q$ value $<1$ indicates that the hologram is operating in the thin regime.

For materials that facilitate a high refractive index modulation during the holographic recording process, the $Q$ parameter becomes insufficient for determining the regime of operation. This is because the assumption that $\nu_\rho = 2\pi\Delta nd/\lambda_r$ remains less than 6 is invalidated [22], where $\nu_\rho$ is the phase accumulation parameter. Instead, a second parameter $\rho$, must be considered. The $\rho$ parameter (Eq. 5), given by Moharam & Young [22], has no thickness dependence:

$$\rho = \frac{\lambda_r^2}{\Lambda^2 n\Delta n} \tag{5}$$

where $\Delta n$ is the refractive index modulation. An intermediate regime exists for conditions such that $1 < Q < 10$ and $1 < \rho < 10$. Here, multiple diffracted orders may appear and the characteristics of the hologram do not explicitly belong in either the volume or thin regimes.

### 2.3. Description of thin gratings

Thin phase holograms are well described by Raman-Nath Theory [23]. When $\Lambda$ is large relative to $d$, several diffracted waves are produced. The diffraction efficiency of thin phase gratings is given by

$$\eta = J_m^2\left(\frac{\varphi}{2}\right) \tag{6}$$

where $\varphi$ is the phase of the grating and $J_m$ is a Bessel function of the first kind, of order $m$. The amplitude of the diffracted beam, in the $m^{th}$ order is proportional to the value of the Bessel function. The definition of $\varphi$ is

$$\varphi = \frac{2\pi\Delta nd}{\lambda_r \cos\theta_B}. \tag{7}$$

### 2.4. Description of volume gratings

Kogelnik's Coupled Wave Theory (KCWT) [24] is used to describe the diffraction characteristics of volume gratings. The diffraction behavior (DE, angular selectivity, and wavelength selectivity) of volume holographic gratings are well described by KCWT. The theory is valid for holograms with high DEs and can be applied to both transmission and reflection holograms. Modulations of refractive index and the absorption constant are accounted for, along with the effects of loss in the grating and slanted fringes. A mismatch constant, $\Gamma$, is introduced to evaluate the effect of deviation away from the Bragg condition [25]. When the Bragg mismatch is due to angular detuning $\Delta\theta$ and wavelength detuning $\Delta\lambda$, the mismatch constant is expressed as

$$\Gamma = \Delta\theta \cdot K\sin(\phi_S - \theta_R) - \frac{\Delta\lambda \cdot K^2}{4\pi n} \tag{8}$$

where $\phi_S$ is the slant angle, $\theta_R$ is the angle of incidence in the material and $K = 2\,\pi/\Lambda$. The DE, $\eta$, for slanted gratings can be calculated by Eq. (9),

$$\eta = \frac{\sin^2\sqrt{\nu^2 + \xi^2}}{1 + \frac{\xi^2}{\nu^2}} \tag{9}$$

where $\nu$ and $\xi$ are given by

$$\nu = \frac{\pi \Lambda \Delta n}{\lambda_r \sqrt{\cos\theta_R \cos\theta_S}}, \tag{10}$$

$$\xi = \frac{\Gamma d}{2\cos\theta_S} \tag{11}$$

and $\theta_S$ is the angle of diffraction in the material. For materials with a known refractive index modulation, changes to the material layer thickness and recording spatial frequency can alter angular selectivity within the grating. Therefore, it is possible to tune the angular sensitivity of HOEs for a given application.

## 3. Materials and methods

### 3.1. *Modelling the gratings*

To determine the holographic recording conditions necessary to record both thin and volume holograms, numerical modelling of both the $Q$ and $\rho$ parameters was carried out. The model was used to calculate the hologram spatial frequency required to record thin and volume holograms, for a given material and layer thickness. The chosen holographic recording medium was the self-developing Bayfol HX200 photopolymer film [26]. Bayfol HX200 has a layer thickness of 16 ± 2 µm, a refractive index modulation ≈ 0.01 for transmission mode holograms, with a spatial frequency of 1000 lines/mm [26], and an average refractive index of 1.505.

Spatial frequencies of 150 lines/mm and 1130 lines/mm for recording the thin and volume versions of the AHWFS, respectively, were chosen from Fig. 2(a). It was important to consider also the angular selectivity of the recorded holograms (Fig. 2(b)). A doubling of the layer thickness resulted in a twofold reduction of the full width at half maximum of the Bragg selectivity curve. By narrowing the range of replay angles of the hologram it is possible to increase the sensitivity of the AHWFS to changes in the incoming wavefront.

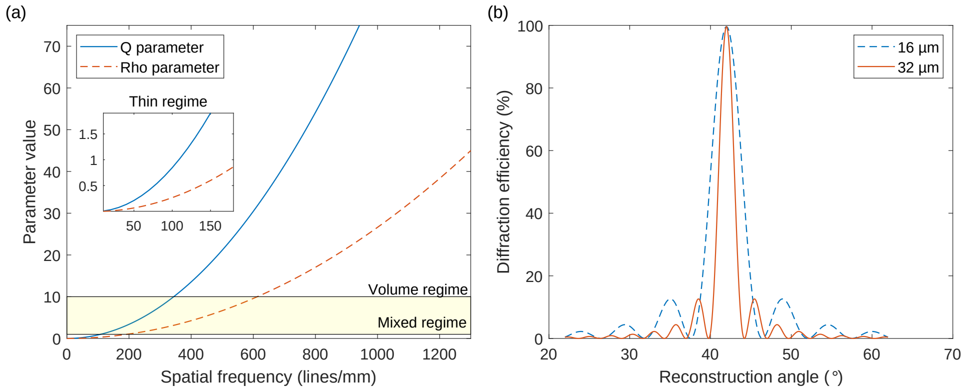

**Fig. 2.** (a) Model of $Q$ and $\rho$ parameters over a spatial frequency range of 0 to 1300 lines/mm for Bayfol HX200 layer thickness of 32 µm. (b) Model of the Bragg selectivity curve, based on KCWT, for Bayfol HX200 layer thicknesses of 16 µm and 32 µm, using a spatial frequency of 1130 lines/mm and $\lambda_r$ = 633 nm.

### 3.2. *Fabrication of holographic gratings*

#### 3.2.1. Optical recording setup

The holographic recording setup was arranged such that the beam from a 633 nm REO HeNe tube laser was expanded to fill the vertical axis (~ 8.6 mm) of a Holoeye PLUTO-2-VIS-016

SLM (Fig. 3). The beam was then split by a 45:55 pellicle beamsplitter. Along the SLM path, the reflected beam, $B_R$, was demagnified to 6.5 mm and imaged onto the holographic recording medium using a 4F imaging system, comprised of achromatic doublet lenses. A series of plane mirrors were used to direct the portion of the beam that was transmitted, $B_T$, towards the holographic recording plane. An aperture was used to reduce the diameter of $B_T$ to 6.5 mm. The two overlapping beams produced the desired interference pattern within the holographic medium, which was then recorded.

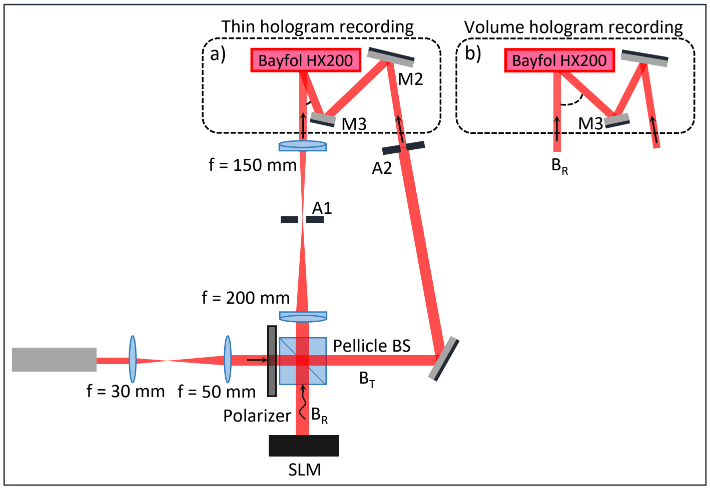

**Fig. 3.** The holographic recording arrangement for fabrication of thin and volume versions of the single-mode AHWFS for measurement of $Z_2^0$. Symbols: SLM: spatial light modulator, M1-4: planar mirrors, A1-2: apertures.

### 3.2.2. Thin holograms

Thin holograms were fabricated with a carrier spatial frequency of 150 lines/mm and a central slant angle of 1.8°. Mirror M2 was rotated to reflect beam $B_T$ onto M3 (Fig. 3) and onto the sample. The full angle between the recording beams was 5.4°, in air. A single layer of Bayfol HX200 was laminated to a glass slide that had been blackened using acrylic paint along the edges and back side. The film was rolled in place, with a rubber ink roller, to eliminate air pockets. A $Z_2^0$ bias of $\pm 1.05$ µm was applied to the SLM. The sample was illuminated for 28 s, with a total recording power of 40 µW/cm$^2$. The recording time was chosen following an iterative process. The sample was then carefully removed from the blackened glass slide and transferred to a transparent glass slide. Given the number of diffraction orders from thin holograms, angular multiplexing risked causing ambiguity in defining the first order spots. Therefore, two separate samples, biased with $+1.05$ µm and $-1.05$ µm of $Z_2^0$ respectively, were holographically recorded.

### 3.2.3. Volume holograms

For recording of a volume phase transmission AHWFS, the position of the mirror M3 was adjusted laterally, and rotated, to increase the angle between the recording beams. M2 (Fig. 3) was rotated to reflect the beam onto M3 and subsequently onto the photopolymer sample. The full angle between the recording beams, in air, was 41.9°. This produced a hologram with a spatial frequency of 1130 lines/mm and a central slant angle of 13.8°. A double layer of Bayfol HX200 was used to produce the volume holograms and the photopolymer sample, on a glass slide, was prepared using the same method as described in 3.2.2. A second layer was laminated on top of the first to increase the overall layer thickness of the recording medium (Fig. 4). By stacking two layers there is an asssumption that the overall effective thickness of the photopolymer medium will be 32 µm and that the recorded holograms will be in the volume regime. It is further assumed reflection and other losses from the cellulose triacetate layer are negligible and the material will behave as one single layer. Finally it is assumed there is minimal compression of the layers, after relaxation, due to the rolling and stacking procedure carried out during sample preparation. The sample was fixed in place with the covered photopolymer layer facing the surface of the beamsplitter. The slide was arranged so that $B_R$ was at normal incidence to the sample. $Z_2^0$, with a Zernike coefficient amplitude of +1.05 µm, was applied to the SLM. A total recording power of 40 µW/cm$^2$, divided equally between the two beams, was used to illuminate the sample for 25 s. The same recording conditions were used to record a second, separate hologram biased with $Z_2^0 = -1.05$ µm. Angular multiplexing or hologram stacking techniques were intentionally not employed, enabling direct comparison of the output from both the volume and thin versions of the sensor.

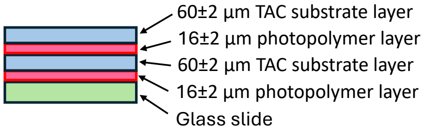

**Fig. 4.** The Bayfol HX200 stack for recording volume holograms.

### 3.3. *Characterization of thin and volume AHWFSs*

#### 3.3.1. Measurement of diffraction efficiency

The DE of the recorded thin and volume holograms was measured by blocking $B_T$ so that only the beam $B_R$ was used in replaying the hologram (Fig. 5). A biconvex lens was placed in the diffracted first order from each HOE to ensure that the full field spot intensity was captured. When the probe beam was phase matched to the beam used to record the hologram of interest, the intensity of the diffracted output of the hologram was maximal. For thin holograms, the beam was separated into many orders. In the volume case, some portion of the beam was transmitted and some diffracted into the first order.

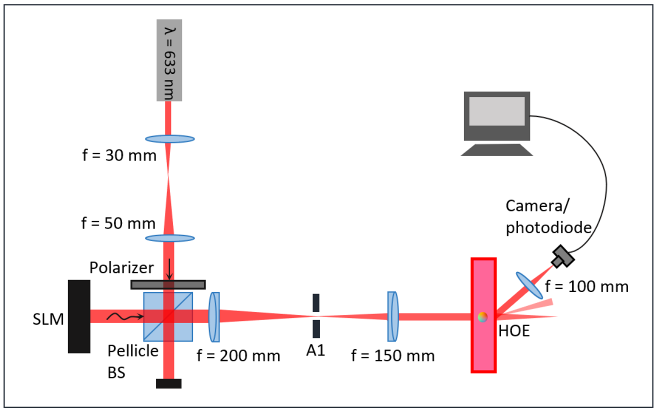

**Fig. 5.** Replay of the HOE biased with $Z_2^0$. A photodiode circuit and an Arduino Due were used to measure the *NIR* produced by each test aberration. This was repeated using a camera in place of the photodiode and Arduino Due.

The DE of the holograms was measured by illuminating either type with the same wavefront that was used to create it. The wavefront of the probe beam was shaped using the SLM. This ensured that that Bragg condition was satisfied. Good equalization of the DE can help to obtain a sensor response that is centered around (0,0). The DE was obtained through a measurement of the intensity of the transmitted beam ($I_T$), the spot for which the Bragg condition was satisfied ($I_{Hj}$), i.e., the first order, and the other diffracted spots ($I_{Hk}$). The efficiency, $\eta$, of the hologram under probe was calculated by Eq. (12),

$$\eta_{Hj} = \frac{I_{Hj}}{I_T + \sum_{k=1}^{k=N} I_{Hk}} \tag{12}$$

where $N$ is the total number of diffracted spots from the HOE and $j$, $k$, and $N \geq 1 \in \mathbb{N}$. A silicon PIN photodiode (Thorlabs FDS1010) with an area of 100 mm$^2$, connected to the analog input of an Arduino Due was used to measure the beam intensities. The DE of the first order from the thin holograms was measured as 21.0% and 20.3%, for +1.05 µm and −1.05 µm respectively. The DE of the volume holograms was measured as 45.1% and 45.9%, for +1.05 µm and −1.05 µm respectively.

### 3.3.2. Evaluation of crosstalk effects with a single additional aberration

The effect of crosstalk on the AHWFS was quantified through measurement of the $Z_2^0$ characteristic curve in the presence of one other aberration. As before, the beam $B_T$ was blocked so that only the beam $B_R$ was incident on the HOE. The SLM was used to produce the wavefront aberrations. Aberrations with magnitudes $Z_2^2 = \pm 0.33$ µm, $Z_3^1 = \pm 0.14$ µm, and $Z_4^0 = \pm 0.14$ µm were applied to the SLM. In addition, $Z_2^0$ magnitudes, in the range ±1.05 µm, were displayed in combination. As discussed in 2.1, the *NIR* from a thin AHWFS must be calculated over an optimized ROI for the chosen bias aberration. Accordingly, a monochrome camera (The Imaging Source DMK33UP1300) was used to capture the diffracted spot profile. Matlab code was used to process the camera images. The camera was positioned such that only the first-order diffracted beam from the holograms was incident on the sensor. No higher orders were captured in the images and the exposure time was adjusted to avoid pixel saturation. A background image, with no diffracted spot present, was taken at each exposure level. The gray values of each image were scaled based on their exposure value and a background subtraction was carried out. A ROI, with a radius given in number of pixels, was used to calculate the *NIR* from the thin and volume AHWFSs (Fig. 6). The centre of the ROI was set to the centre of mass across the diameter of the

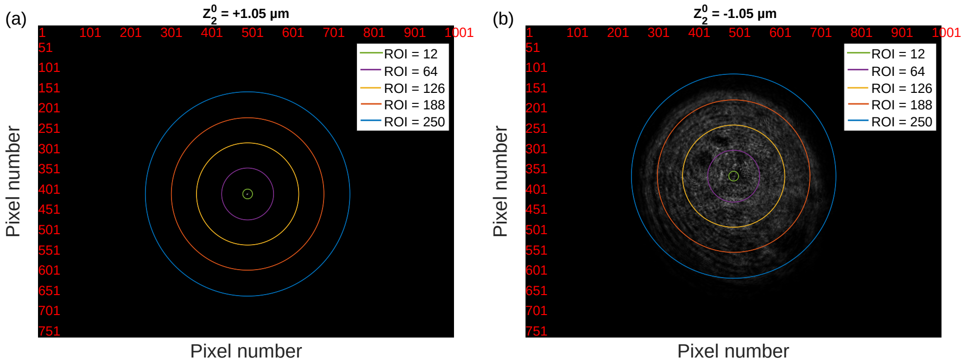

**Fig. 6.** The camera ROIs, given in pixel radius, used to analyze the diffracted first order beams from both thin and volume holograms replayed with (a) $Z_2^0$ = +1.05 µm, and (b) $Z_2^0$ = −1.05 µm.

detector. This calculation was carried out for a number of ROIs, to examine the influence of ROI on the effect of crosstalk for a single additional aberration mode.

A reduction in the radius of the ROI caused an increase in the slope of the characteristic curve for $Z_2^0$ (Fig. 7). In this way, the sensitivity and linearity of the AHWFS can be tuned. Subsequently, the crosstalk measurements were carried out using the photodiode and Arduino Due. The photodiode was used to measure the intensity of the first-order diffracted beams from the volume AHWFS only. The effect of crosstalk, as was analyzed by camera measurements, was compared to crosstalk analysis derived from photodiode measurements.

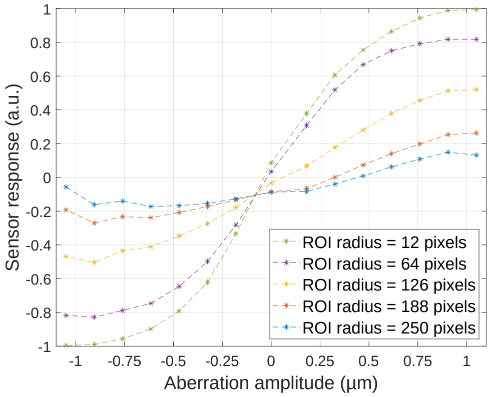

**Fig. 7.** The *NIR* for $Z_2^0$, from the diffracted output of a volume AHWFS, calculated over ROIs with radii: 12, 64, 126, 188, and 250 pixels.

### 3.3.3. Evaluation of crosstalk effects with multiple additional aberrations

AO for free-space optical communication (FSOC) is one of the targeted applications of the HWFS. Inhomogeneities in the refractive index of the atmosphere are caused mostly by temperature variations. Many low-order and high-order aberrations are introduced as the wavefront propagates through this atmospheric turbulence. Therefore, it is important to investigate the effect of crosstalk on the HWFS in the presence of multiple aberration modes. Computer generated phase screens were used to emulate atmospheric turbulence conditions with a strength of $D/r_0 = 10$, where $D$ is the diameter of the receiving telescope and $r_0$ is the transverse coherence length of the wavefronts after traversing through emulated turbulence (Fried parameter). The first 11 Zernike aberration modes following the turbulence statistics, after $Z_1^1$, $Z_1^{-1}$, and $Z_2^0$ were extracted from 50 uncorrelated phase screens. A fixed magnitude of $Z_2^0 = 0.27$ μm (2.69 rad) was applied to the SLM in combination with each of the Zernike mode sets. The thin and volume AHWFSs were used to continually measure $Z_2^0$ as the other 11 modes were updated. The standard deviation of 50 measurements of $Z_2^0$ from each sensor was used to determine the effect of crosstalk. The measurements were first carried out with a camera and software-defined ROI for both the thin and volume AHWFSs. The measurements were repeated for the volume sensor using a photodiode to capture the diffracted spot intensity.

## 4. Results

### 4.1. *Measurement of crosstalk effects with a single additional aberration*

### 4.1.1. Thin holograms

The holograms were replayed with $Z_2^0$ in the range ±1.05 μm and the characteristic curve was determined at ROI radii of 12, 64, 126, 188, and 250 pixels. The *NIR* was calculated by Eq. (1)

and plotted against the magnitude of $Z_2^0$ to be measured. The slope of the linear portion of the graph was determined and the sensor response was calculated by Eq. (2). The holograms were then replayed with $Z_2^0$ in combination with the aberrations mentioned previously ($Z_2^2$, $Z_3^1$, and $Z_4^0$) (Fig. 8). The measurement error was quantified as the absolute difference between the characteristic curve for $Z_2^0$ and the curves obtained in the presence of one other aberration (see Visualization 1, Visualization 2 and Visualization 3). When the ROI was large, ≥ 126 pixels, the crosstalk effect from the presence of one other aberration was low (< 0.06 μm) (Fig. 8(a)-(d)). However, as the ROI was reduced, the effect of crosstalk, particularly from $Z_4^0$, was considerable (Fig. 8(e), (f)). The maximum deviation from the reference curve was 1.53 μm, for a ROI radius of 12 pixels, with the introduction of $Z_4^0 = -0.14$ μm.

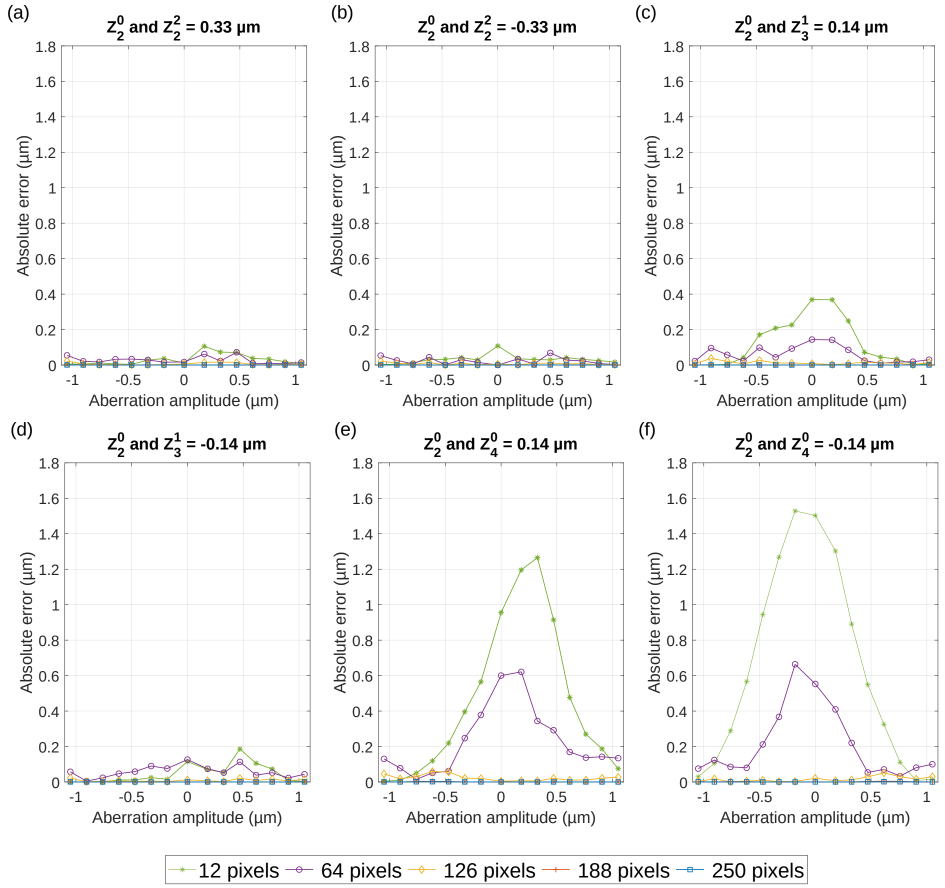

**Fig. 8.** The absolute error, measured as the difference between the characteristic curve for $Z_2^0$ and $Z_2^0$ in combination with: (a) $Z_2^2 = 0.33$ μm, (b) $Z_2^2 = -0.33$ μm, (c) $Z_3^1 = 0.14$ μm, (d) $Z_3^1 = -0.14$ μm, (e) $Z_4^0 = 0.14$ μm, (f) $Z_4^0 = -0.14$ μm, for the first order diffracted beam from a thin AHWFS. The sensor output was measured with a camera and calculated over ROIs with radii: 12, 64, 126, 188, and 250 pixels.

#### 4.1.2. Volume holograms

The volume holograms, biased with $Z_2^0 = \pm 1.05$ μm were replayed first with $Z_2^0$ only to determine the characteristic curves and then in combination with one other aberration mode: $Z_2^2 = \pm 0.33$ μm, $Z_3^1 = \pm 0.14$ μm, and $Z_4^0 = \pm 0.14$ μm (Fig. 9). Software ROIs of 12, 64, 126, 188, and 250 pixels were applied to the camera images in order to calculate the *NIR*. Again, when the ROI was ≥ 126 pixels, the crosstalk effect from the presence of one other aberration was low (< 0.12 µm) (Fig. 9(a)-(d)). However, when one additional aberration mode was present the effect of crosstalk was greater as the ROI radius was reduced (Fig. 9(e), (f)). The maximum deviation from the reference curve was 1.74 µm, for a ROI radius of 12 pixels, with the introduction of $Z_4^0 = -0.14$ µm (see Visualization 4, Visualization 5 and Visualization 6). In general, the thin AHWFS performed better than the volume AHWFS for measuring defocus in the presence of one additional aberration mode.

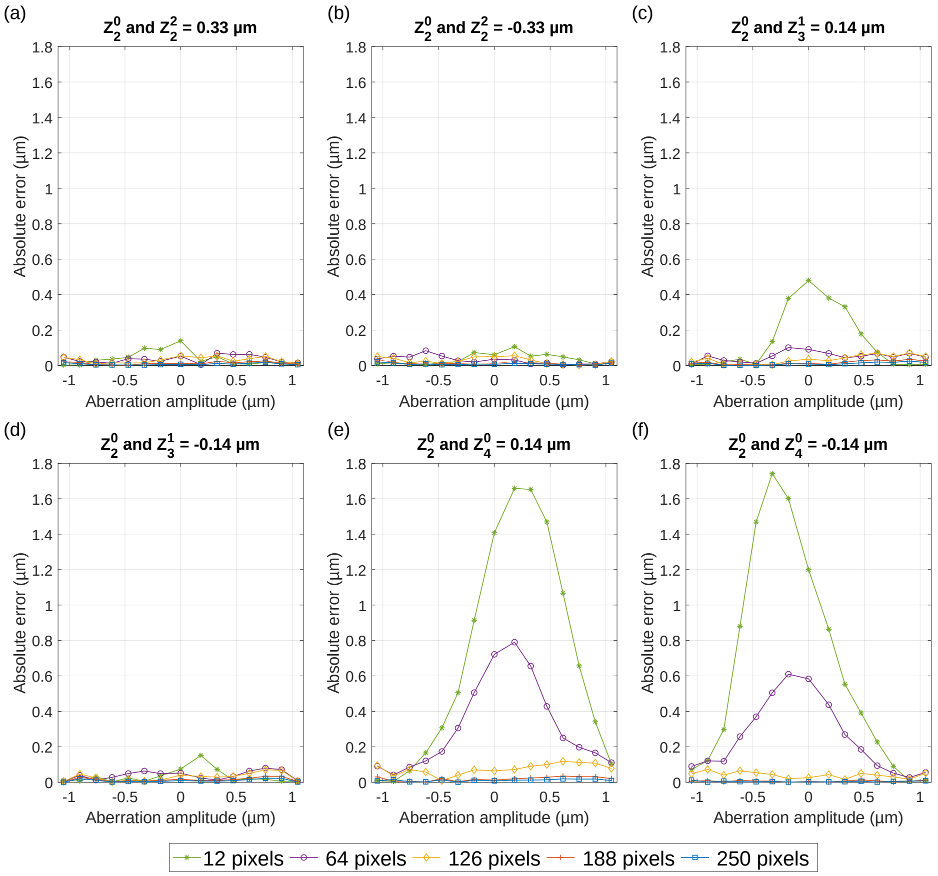

**Fig. 9.** Again, the absolute error was calculated for a volume AHWFS for measurement of $Z_2^0$ in combination with: (a) $Z_2^2 = 0.33$ µm, (b) $Z_2^2 = -0.33$ µm, (c) $Z_3^1 = 0.14$ µm, (d) $Z_3^1 = -0.14$ µm, (e) $Z_4^0 = 0.14$ µm, (f) $Z_4^0 = -0.14$ µm over ROIs with radii: 12, 64, 126, 188, and 250 pixels.

The sensitivity (Fig. 10) of the thin and volume AHWFSs was evaluated, through calculation of the slope of each characteristic curve for a chosen detection ROI. The slopes were obtained from the curves corresponding to $Z_2^0$ only. The optimum ROI for the thin and volume AHWFSs was 22 and 42 pixels, with $m_{CC}$ values of 1.84 µm$^{-1}$ and 2.08 µm$^{-1}$ respectively.

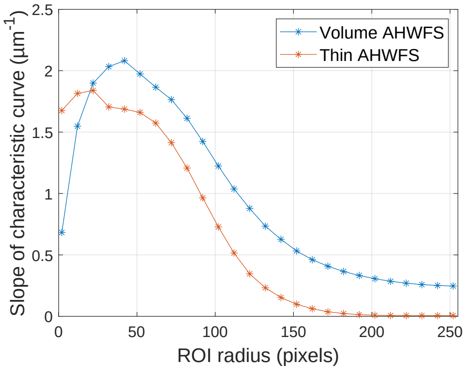

**Fig. 10.** Slopes of $Z_2^0$ characteristic curves for thin and volume AHWFSs, at various ROI radii.

### 4.1.3. Comparison with photodiode measurements

The volume AHWFS was replayed with $Z_2^0$ in the range ±1.05 µm (Fig. 11(a)) and then in combination with one other aberration mode: $Z_2^2 = \pm 0.33$ µm, $Z_3^1 = \pm 0.14$ µm, and $Z_4^0 = \pm 0.14$ µm (Fig. 11(b)-(d)). The diffracted first order spot intensity of the volume AHWFS

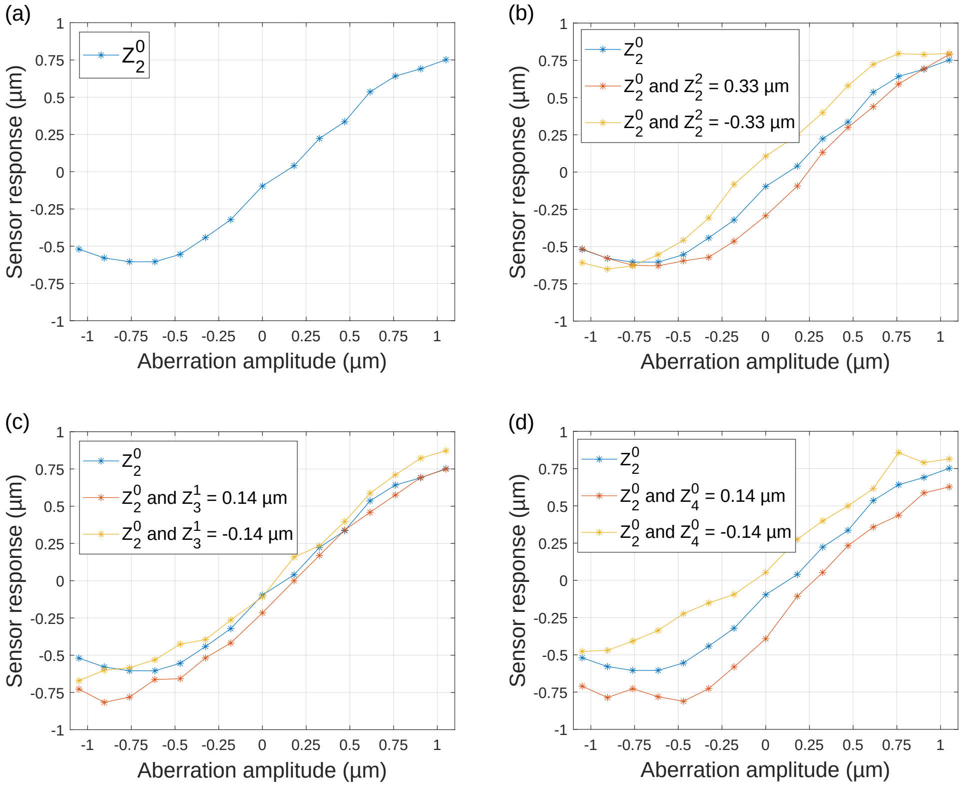

**Fig. 11.** The characteristic curves for $Z_2^0$ obtained from a photodiode measurement of the diffracted output of a volume AHWFS, when reconstructed with (a) $Z_2^0$, (b) $Z_2^0$ and $Z_2^2 = \pm 0.33$ µm, (c) $Z_2^0$ and $Z_3^1 = \pm 0.14$ µm, and (d) $Z_2^0$ and $Z_4^0 = \pm 0.14$ µm.

was measured using a photodiode and an Arduino Due to obtain the characteristic curve.

The introduction of +0.14 µm and −0.14 µm of $Z_4^0$ resulted in a maximum error of 0.30 µm and 0.33 µm respectively. Taking the largest ROI radius, 250 pixels, a comparison between the measurement with the camera or photodiode can be made, as the full field intensity of the diffracted beam is captured by both. Overall, the effect of crosstalk was lower for curves captured using the camera. The maximum error was 0.03 µm (ROI radius = 250 pixels). Background subtraction may have been a contributing factor to the reduced error measured with the camera. It was previously observed that a change in background intensity can cause the characteristic curve to translate along the y-axis. Improvements to the photodiode measurement may be possible by carrying out an intermittent background intensity measurement and subsequent field subtraction.

### 4.2. Measurement of crosstalk effects with multiple aberrations present

A fixed magnitude of $Z_2^0$, 0.27 µm (2.69 rad), was measured through emulated atmospheric turbulence, with strength $D/r_0 = 10$. This measurement was carried out 50 times, with the introduction of each new set of aberration magnitudes associated with the given turbulence statistics. The first-order diffracted beams from the thin and volume wavefront sensing holograms were captured using a camera and the $NIR$, $m_{CC}$, and $W_D$ were calculated as previously. The standard deviation of these measurements was then calculated for each software ROI (Fig. 12). This was used to evaluate the WFS measurement error. The optimum ROI, for the lowest standard deviation on the measurement, was 82 and 42 pixels for the thin and volume sensors, respectively. The standard deviation at these ROIs was 0.25 and 0.21 rad. Measurements were also carried out using a photodiode for the volume AHWFS, which were comparable to measurements carried out over a large ROI on the camera as the full field intensity of the diffracted output was analyzed. For a ROI of 252 pixels, the standard deviation was 0.64 rad, while the standard deviation of the photodiode measurement was 0.78 rad.

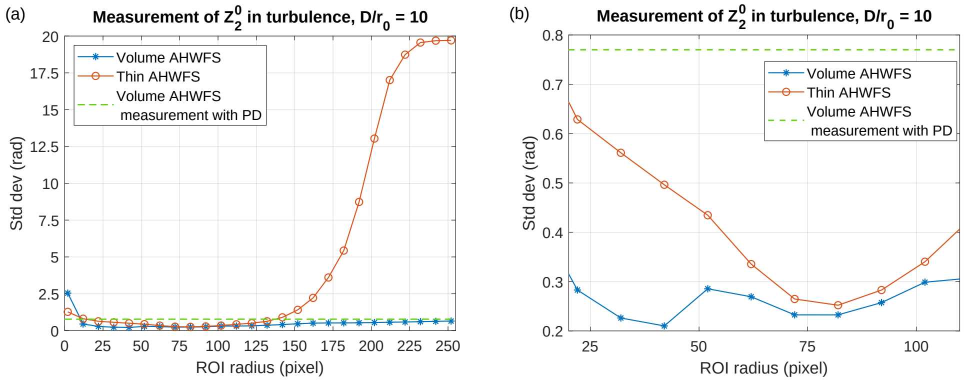

**Fig. 12.** Measurement of a fixed magnitude of $Z_2^0$ by a thin and volume AHWFS through emulated atmospheric turbulence, with strength $D/r_0 = 10$, for ROIs with radius (a) 2 - 252 pixels and (b) 22 - 102 pixels.

Although the minimum standard deviation for a volume HWFS is lower than for a thin HWFS (Fig. 12), in principle it was observed that both types of holograms can achieve comparable measurement accuracy. However, the key observation is that the performance of a volume HWFS is constant whereas the performance of a thin HWFS strongly depends on the selected ROI. There are several considerations that should be accounted for when choosing the operating regime of a HWFS.

**i)** The crosstalk of a thin HWFS can be significantly reduced by selecting the appropriate ROI. The crosstalk of a volume HWFS depends much less on the choice of ROI. Accordingly, measurement accuracy is not the sole criterion when selecting the ROI for a volume HWFS. Instead, other sensor properties such as sensitivity (Fig. 10) should also be taken into account and optimized when designing the sensor.

**ii)** If the magnitude or modal composition of the aberrations evolves beyond expected bounds, then the accuracy of HWFS based on thin holograms decreases but the accuracy of the volume sensor is not affected. This means that the volume sensor is more tolerant to changes of atmospheric conditions. For volume holograms, it is not necessary to adjust the ROI to the turbulence strength. HWFSs based on volume holograms can be easily implemented with fixed aperture masks in front of fast photodiode arrays. However, for a thin HWFS an optimum ROI must be found for the prevailing atmospheric conditions to achieve acceptable measurement accuracy [19], with the size of the ROI adjusted accordingly. A flexible sensor design is therefore necessary to make the thin holographic sensor suitable for a larger turbulence range. When using a camera, this can easily be realized by a software-defined ROI. When using a photodiode array to benefit from the fast readout speed, the implementation is much more complex.

**iii)** The high photon efficiency of a *full-light mode* is of particular benefit for photon-starved scenarios, meaning that all of the light in the diffraction order of interest is captured. HWFSs based on volume holograms can be operated in full-light mode. HWFSs based on thin holograms cannot be operated in full-light mode as a rather small ROI is mandatory to achieve reasonable sensitivity and accuracy. For a volume sensor, the focused spots in the detector plane do not have to be cropped by the ROI. Figures 10 and 11 show that even for a ROI containing the whole spots, the sensitivity, as well as the accuracy is acceptable for closed-loop AO applications.

**iv**) The photodiode that was used in this study has a rise/fall time of 65 ns. When operating at the maximum capacity of the photodiode and Arduino Due, the wavefront can be measured at speeds ~1 MHz. The camera used in this work has a frame rate of 210 fps. In the visible spectral range, there exist CCD and sCMOS detectors that can deliver frame rates of several kHz in full-frame mode. However, in short-wave infrared, which is the preferred spectral range for FSOC, there exists an even larger gap between the frame rates of area detectors (typically less than 1 kHz full frame) and photodiodes (~1 GHz). This is one major advantage to using a photodiode array and a volume hologram over a thin hologram and a camera.

Regarding practical implementations, a sensor capable of measuring multiple aberration modes simultaneously is required. This can be fabricated by holographically multiplexing many modes into the HWFS. With a volume AHWFS, only one diffracted order is present for each recorded hologram. For a thin AHWFS, many diffracted orders are present for each hologram that is recorded. As the number of aberration modes increases, the diffracted output becomes complex, difficult to analyze, and potentially more prone to both inter- and intra-modal crosstalk. It should be noted that fabrication of analog holograms presents several challenges. Shrinkage of common holographic recording materials such as photopolymers [17,27], silver halide, and dichromated gelatin is a problem encountered when multiplexing many modes into one device. To obtain the angular selectivity required to sense higher-order aberration modes when using a volume AHWFS, the spatial frequency or the thickness of the recording layer must be increased. However, with an increase in angular selectivity the effect of material shrinkage on the diffracted output from the sensor is greater [9].

## 5. Conclusion

In this work, thin and volume analog holograms were produced in a self-developing photopolymer for wavefront sensing. This is the first time that a direct comparison of the crosstalk performance of both thin and volume AHWFSs has been made. The characteristic curves for $Z_2^0$ were obtained through a normalized intensity measurement of the diffracted first-order beam of the holograms, using a camera and a software-defined region of interest. Measurements of $Z_2^0$ in the presence of $Z_2^2$, $Z_3^1$, and $Z_4^0$ were carried out. The impact of crosstalk, from one additional aberration, on the sensor measurement was lower overall for the thin AHWFS than the volume AHWFS. When the detection ROI radius ≥ 126 pixels, the maximum absolute error on the measurement of defocus was 0.06 μm and 0.12 μm for the thin and volume sensors respectively. The presence of ±0.14 μm of $Z_4^0$, in combination with an ROI radius of 12 pixels had the greatest impact on measurement accuracy. It was possible to directly compare two methods of obtaining the sensor response from a volume AHWFS, first using a camera and software ROI and then with a photodiode. This was not the case for the thin AHWFS, as a reduction in the size of the ROI was necessary to obtain a characteristic curve. In general, the absolute error on the measurement of $Z_2^0$ in the presence of one additional aberration was higher when carried out using a photodiode.

A fixed magnitude of $Z_2^0$ (0.27 μm or 2.69 rad) was measured 50 times through emulated atmospheric turbulence conditions, with a strength of $D/r_0 = 10$. The standard deviation on measurements carried out with the thin and volume AHWFS was 0.25 and 0.21 rad respectively. The performance of the volume AHWFS did not degrade significantly with an increase in the ROI radius. However, the thin AHWFS became unusable when the entirety of the diffracted beam was used to calculate the sensor response. A photodiode was also used to capture the sensor response from the volume AHWFS. A standard deviation of 0.77 rad was calculated on the measurements performed using the photodiode. This measurement highlighted the speed and photon efficiency advantages of using a volume AHWFS for wavefront sensing in turbulent conditions. A number of considerations for choosing AHWFS type in terms of detector speed, available light, and complexity were presented.

**Funding.** Science Foundation Ireland (18/SIRG/5666); Irish Research eLibrary.

**Acknowledgments.** The authors would like to acknowledge colleagues in IEO for useful guidance and constructive conversations. Open access funding provided by Irish Research eLibrary.

**Author contributions**. KM obtained funding for, and supervised direction of, the project; all authors contributed to the experimental plan; EB carried out all experimental work; EB, AZ, & KM contributed to the data analysis; EB produced all Figures; EB drafted the initial manuscript; KM, SM, MS, AZ & SG edited the manuscript. Open access funding provided by Irish Research eLibrary.

**Disclosures.** The authors declare that there are no conflicts of interest related to this article.

**Data availability.** Data underlying the results presented in this paper are not publicly available at this time but may be obtained from the authors upon reasonable request.

## References

1. M. A. A. Neil, M. J. Booth, and T. Wilson, “Closed-loop aberration correction by use of a modal Zernike wave-front sensor,” Opt. Lett. **25**(15), 1083 (2000).
2. M. J. Booth, “Direct measurement of Zernike aberration modes with a modal wavefront sensor,” Proc. SPIE **5162**, 1 (2003).
3. G. Andersen, F. Ghebremichael, R. Gaddipati, *et al.*, “Fast computer-free holographic adaptive optics,” Proc. SPIE **8447**, 84472L–84472L-8 (2012).
4. G. Andersen, P. Gelsinger-Austin, R. Gaddipati, *et al.*, “Fast, compact, autonomous holographic adaptive optics,” Opt. Express **22**(8), 9432–9441 (2014).
5. F. Ghebremichael, G. P. Andersen, and K. S. Gurley, “Holography-based wavefront sensing,” Appl. Opt. **47**(4), A62–A69 (2008).
6. A. Zepp and S. Gladysz, “Fast defocus measurement for laser communications with the holographic wavefront sensor,” in *Imaging and Applied Optics* (2013), paper OTu1A.5.
7. A. Zepp, S. Gladysz, R. Barros, *et al.*, “Analogue holographic wavefront sensor: a performance analysis,” Proc. SPIE **9614**, 9614G (2015).
8. F. Kong and A. Lambert, “Improvements to the modal holographic wavefront sensor,” Appl. Opt. **55**(13), 3615 (2016).
9. E. Branigan, S. Martin, M. Sheehan, *et al.*, “An analog holographic wavefront sensor for defocus and spherical aberration detection recorded in a photopolymer,” Opt. Express **31**(6), 9466–9480 (2023).
10. G. P. Andersen, L. C. Dussan, F. Ghebremichael, *et al.*, “Holographic wavefront sensor,” Opt. Eng. **48**(8), 085801 (2009).
11. G. Krasin, N. Stsepuro, I. Gritsenko, *et al.*, “Holographic method for precise measurement of wavefront aberrations,” Proc. SPIE **11774**, 1177407 (2021).
12. C. Liu, T. Men, R. Xu, *et al.*, “Analysis and demonstration of multiplexed phase computer-generated hologram for modal wavefront sensing,” Optik **125**(11), 2602–2607 (2014).

13. P. Marin Palomo, A. Zepp, and S. Gladysz, "Characterization of the digital holographic wavefront sensor," Proc. SPIE **9242**, 92421T (2014).
14. M. S. Kovalev, G. K. Krasin, S. B. Odinokov, *et al.*, "Measurement of wavefront curvature using computer-generated holograms," Opt. Express **27**(2), 1563–1568 (2019).
15. G. Andersen, F. Ghebremichael, and K. Gurley, "Holographic Wavefront Sensor," in *Advanced Maui Optical and Space Surveillance Technologies Conference* (2007).
16. A. Zepp, S. Gladysz, and K. Stein, "Holographic wavefront sensor for fast defocus measurement," Adv. Opt. Technol. **2**(5-6), 433–437 (2013).
17. E. Branigan, S. Martin, M. Sheehan, *et al.*, "Direct multiplexing of low order aberration modes in a photopolymer-based holographic element for analog holographic wavefront sensing," Proc. SPIE **11860**, 118600H (2021).
18. K. Gavril'eva, A. Gorelaya, E. Fedorov, *et al.*, "Approaches to cross-talk noise reduction in modal holographic wavefront sensors," Proc. SPIE **10680**, 106802O (2018).
19. A. Zepp, S. Gladysz, K. Stein, *et al.*, "Simulation-based design optimization of the holographic wavefront sensor in closed-loop adaptive optics," Light: Adv. Manufact. **3**(3), 1 (2022).
20. P. Hariharan, *Basics of Holography* (Cambridge University, 2002) Chap. 3.
21. W. R. Klein and B. D. Cook, "Unified Approach to Ultrasonic Light Diffraction," IEEE Trans. Son. Ultrason. **14**(3), 123–134 (1967).
22. M. G. Moharam and L. Young, "Criterion for Bragg and Raman-Nath diffraction regimes," Appl. Opt. **17**(11), 1757–1759 (1978).
23. N. S. Nagendra Nath, "The diffraction of light by supersonic waves," Proc. Indian Acad. Sci. (Math. Sci.) **8**(5), 499–503 (1938).
24. H. Kogelnik, "Coupled Wave Theory for Thick Hologram Gratings," Bell Syst. Tech. J. **48**(9), 2909–2947 (1969).
25. N. Kim, Y.-L. Piao, H.-Y. Wu, *et al.*, *Holographic Optical Elements and Application* (IntechOpen, 2017) Chap. 5.
26. F.-K. Bruder, T. Fäcke, and T. Rölle, "The Chemistry and Physics of Bayfol® HX Film Holographic Photopolymer," Polymers **9**(10), 472 (2017).
27. M. Moothanchery, I. Naydenova, and V. Toal, "Studies of shrinkage as a result of holographic recording in acrylamide-based photopolymer film," Appl. Phys. A **104**(3), 899–902 (2011).